RESEARCH ARTICLE

annalen der physik
www.ann-phys.org

Zero-Field Hybridization of Anomalous Nernst and Off-diagonal Seebeck Effects in Artificially Tilted Multilayers

Yebin Lee, Fuyuki Ando, Takamasa Hirai, Rajkumar Modak, Hossein Sepehri-Amin, and Ken-ichi Uchida**

Hybrid transverse thermoelectric conversion driven by simultaneous action of multiple phenomena offers a promising route for efficient energy conversion. This study demonstrates magnetic-field-free hybrid transverse thermoelectric conversion based on the anomalous Nernst and off-diagonal Seebeck effects in artificially tilted multilayers comprising $SmCo_5/Bi_{0.2}Sb_{1.8}Te_3$ junctions, where the remanent magnetization of $SmCo_5$ induces the anomalous Nernst effect in the absence of an external magnetic field. The thermoelectric figure of merit is observed to be 0.299 ± 0.005 at room temperature owing to the additive contribution of the anomalous Nernst effect, indicating that the excellent figure of merit due to the off-diagonal Seebeck effect can further be enhanced by hybridizing the anomalous Nernst effect. These results establish a new approach for high-performance transverse thermoelectric materials, enabling energy harvesting and cooling applications that leverage magnetically controlled thermoelectric effects without requiring an external magnetic field.

1. Introduction

Thermoelectric materials enable the direct interconversion of a heat current $\mathbf{J}_q$ into a charge current $\mathbf{J}_c$ and have been extensively studied for their potential in energy harvesting and thermal management applications.[1–3] Conventional thermoelectrics is based on the longitudinal Seebeck and Peltier effects, where $\mathbf{J}_q$ and $\mathbf{J}_c$ flow in the same direction. To maximize the thermoelectric output, Seebeck/Peltier-effect-based devices are usually constructed with alternately arranging *p*- and *n*-type materials and connecting them in series. The complex structure required for such devices introduces challenges, including low mechanical durability and energy losses due to contact resistances at the junctions.[4] Transverse thermoelectric effects, by contrast, enable the interconversion of $\mathbf{J}_q$ and $\mathbf{J}_c$ in orthogonal directions, offering a simplified architecture. By eliminating substrates and junctions, transverse thermoelectrics can increase thermoelectric conversion efficiency and reduce energy losses, thus addressing the limitations of longitudinal thermoelectric devices.[5]

Transverse thermoelectric conversion is driven by various mechanisms including the ordinary/anomalous Nernst effect (ONE/ANE)[6–13] induced by a magnetic field/spontaneous magnetization and the off-diagonal Seebeck/Peltier effect (ODSE/ODPE). ODSE and ANE are the thermoelectric generation effects that induce $\mathbf{J}_c$ perpendicular to the applied temperature gradient. In contrast, ODPE and the anomalous Ettingshausen effect (AEE) are the Onsager reciprocals of ODSE and ANE, respectively, that induce $\mathbf{J}_q$ perpendicular to the applied charge current. ODSE/ODPE occurs in anisotropic crystals[14–18] and artificially tilted multilayers (ATMLs),[19–34] which consist of two conductors alternately and obliquely stacked. Recently, hybridization of the multiple transverse thermoelectric effects in ATMLs has been demonstrated as a promising approach for the realization of giant transverse thermoelectric conversion.[32,33] Combining ODSE with ONE/ANE can provide improved thermoelectric performance beyond what can be achieved with ONE/ANE alone.[32,33] However, this approach typically requires the application of an external magnetic field to drive ONE/ANE, limiting practical applications. Although ANE can occur in the absence of a magnetic field in hard magnetic materials, in previous studies, either soft magnetic materials were used or the remanent magnetization direction in permanent-magnet-based ATMLs did not satisfy the symmetry of ANE; hybridization of ANE in ATMLs in the absence of a magnetic field has not been achieved so far.[32–34] Additionally, the experimentally determined transverse thermoelectric figure of merit in ATMLs remains below 0.20 due to unoptimized ODSE and/or performance degradation due

Y. Lee, F. Ando, T. Hirai, R. Modak, H. Sepehri-Amin, K. Uchida
National Institute for Materials Science
Tsukuba 305-0047, Japan
E-mail: ANDO.Fuyuki@nims.go.jp; UCHIDA.Kenichi@nims.go.jp
Y. Lee, K. Uchida
Graduate School of Science and Technology
University of Tsukuba
Tsukuba 305-8573, Japan
R. Modak, K. Uchida
Department of Advanced Materials Science
Graduate School of Frontier Sciences
The University of Tokyo
Kashiwa 277-8561, Japan

The ORCID identification number(s) for the author(s) of this article can be found under https://doi.org/10.1002/andp.202500127

DOI: 10.1002/andp.202500127

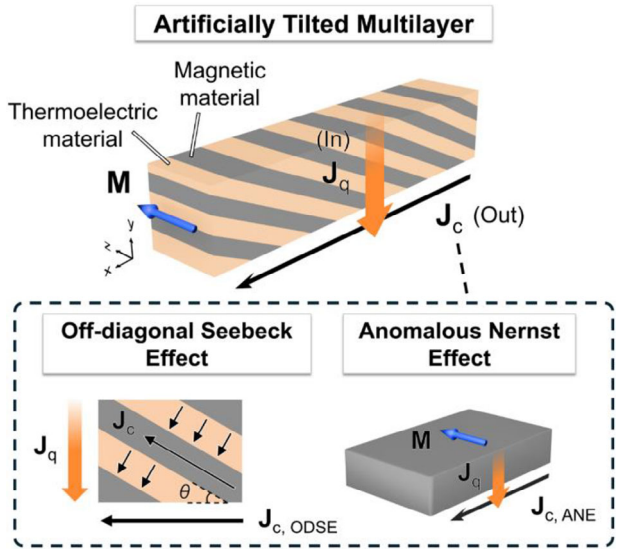

Figure 1. Schematic illustration of transverse thermoelectric conversion in an artificially tilted multilayer (ATML) composed of magnetic and thermoelectric materials. The magnetic materials used in this study, the $SmCo_5$ slabs, have the large anisotropy with an in-plane magnetic easy axis. The heat current $\mathbf{J}_q$ flows along the *y* direction, generating a charge current $\mathbf{J}_c$ along the *x* direction. The off-diagonal Seebeck effect (ODSE) arises from the ATML structure with the tilt angle θ, while the anomalous Nernst effect (ANE) occurs depending on the magnetization **M** in the magnetic materials.

to interfacial electrical/thermal resistances.[34] Addressing these challenges requires materials and structural designs that effectively exploit hybrid transverse thermoelectric conversion at zero field.[35–37]

The effectiveness of the hybrid transverse thermoelectric conversion can be found in the figure of merit $z_{xy}T$ ($= {S_{xy}}^2\sigma_{xx}T/\kappa_{yy}$), where S_{xy}, σ_{xx}, and κ_{yy} respectively denote the transverse thermopower, electrical conductivity along the *x* direction, and thermal conductivity along the *y* direction for ATML. According to Ref. [33], for ANE-hybridized ATML systems, the total transverse thermopower consists of the contributions from ODSE and ANE: $S_{xy} = S_{ODSE} + \hat{S}_{ANE}$ and $z_{xy}T \propto {S_{xy}}^2 = {S_{ODSE}}^2 + 2S_{ODSE}\hat{S}_{ANE} + {\hat{S}_{ANE}}^2$. Here, S_{ODSE} represents the transverse thermopower due to ODSE and $\hat{S}_{ANE}$ is the effective anomalous Nernst coefficient considering the reduction due to the shunting effect. The key point is that the hybridization of ODSE and ANE generates the additional $2S_{ODSE}\hat{S}_{ANE}$ term, leading to a larger ANE-induced $z_{xy}T$ enhancement than what ANE alone can achieve, especially when ODSE is large. This explains why our ATMLs are fundamentally designed to optimize ODSE.

In this study, we demonstrate high-performance transverse thermoelectric conversion based on the hybridization of ODSE and ANE in ATML at zero field (**Figure 1**). Using a lock-in thermography (LIT) method, we directly observe a temperature modulation through the transverse thermoelectric conversion and clarify the contributions from the reciprocal effects of ODSE and ANE independently. The enhancement of the transverse thermoelectric performance is quantified by direct transverse thermopower measurements; the transverse figure of merit for our ATML reaches ≈0.3 at room temperature owing to the large ODSE contribution and the superposition of the ANE contribution.

2. Experimental Section

This study used ATML consisting of $SmCo_5$-type permanent magnets exhibiting large ANE[9,11] and $Bi_{0.2}Sb_{1.8}Te_3$ thermoelectric materials exhibiting the large Seebeck effect. This ATML was similar to that used in Ref. [34] and known to exhibit large ODSE. However, the magnetization direction of the $SmCo_5$ slabs in the ATML was different from that in the previous system. Although the magnetic easy axis of the $SmCo_5$ slabs in the previous system was perpendicular to the stacking plane, the $SmCo_5$ slabs used in this study have the easy axis along the in-plane direction. Thus, in the configuration depicted in Figure 1 where a temperature gradient was applied in the *y* direction, both ODSE and ANE could generate a charge current in the *x* direction.[33] Owing to the large remanent magnetization and coercivity of the $SmCo_5$ slabs, the ATML enables the utilization of ANE without applying an external magnetic field.

The $SmCo_5/Bi_{0.2}Sb_{1.8}Te_3$-based ATML was prepared as follows. The $SmCo_5$ slabs (available from Magfine Corporation, Japan) and BiSbTe alloy powders (available from Toshima Manufacturing Co., Ltd.) were alternately stacked and bonded by spark plasma sintering under a pressure of 30 MPa at 450 °C for 30 min. The $SmCo_5$ slabs were used as delivered without additional processing. The sintered multilayer stack was cut into rectangular shapes with a tile angle of 25° for LIT measurements (≈10.0 × 2.0 × 2.0 mm^3) and thermopower measurements (13.5 × 10.3 × 1.0 mm^3). Note that $z_{xy}T$ was evaluated using the latter sample employed for the thermopower measurements. The tilt angle was determined by the method described later. Then, the magnetization of the rectangular samples was aligned along the magnetic easy axis at room temperature using a superconducting magnet. The composition of the $SmCo_5$ slabs was confirmed to be stoichiometric through inductively coupled plasma analysis. The composition of the $Bi_{0.2}Sb_{1.8}Te_3$ slabs prepared under the same sintering condition was confirmed in the previous study.[34] Electron backscatter diffraction (EBSD) analysis was conducted using a Crossbeam 550 instrument (Carl Zeiss AG) equipped with an EBSD detector. The $SmCo_5$ slabs for EBSD analysis were prepared by mechanical polishing.

The LIT method was used to directly measure the transverse thermoelectric conversion in $SmCo_5/Bi_{0.2}Sb_{1.8}Te_3$-based ATML. The LIT method is an infrared thermometry technique that enables visualization of the spatial distribution and temporal response of temperature modulation induced by an applied charge current with high temperature and spatial resolutions.[38–40] In the LIT measurements, heating and cooling signals oscillating at the same frequency as the applied periodic charge current were captured as thermal images. The LIT measurements were performed by applying a square-wave-modulated ac charge current with an amplitude of 1 A, frequency *f* range of 0.1–10.0 Hz, and zero offset to the sample along its longitudinal direction (*x* direction in Figure 1). The resulting thermal images were converted into lock-in amplitude *A* and phase ϕ images through Fourier analysis. By extracting the first harmonic component of these images, the contribution of the thermoelectric effects ($\propto J_c$, where J_c is the amplitude of J_c) could be distinguished from that of

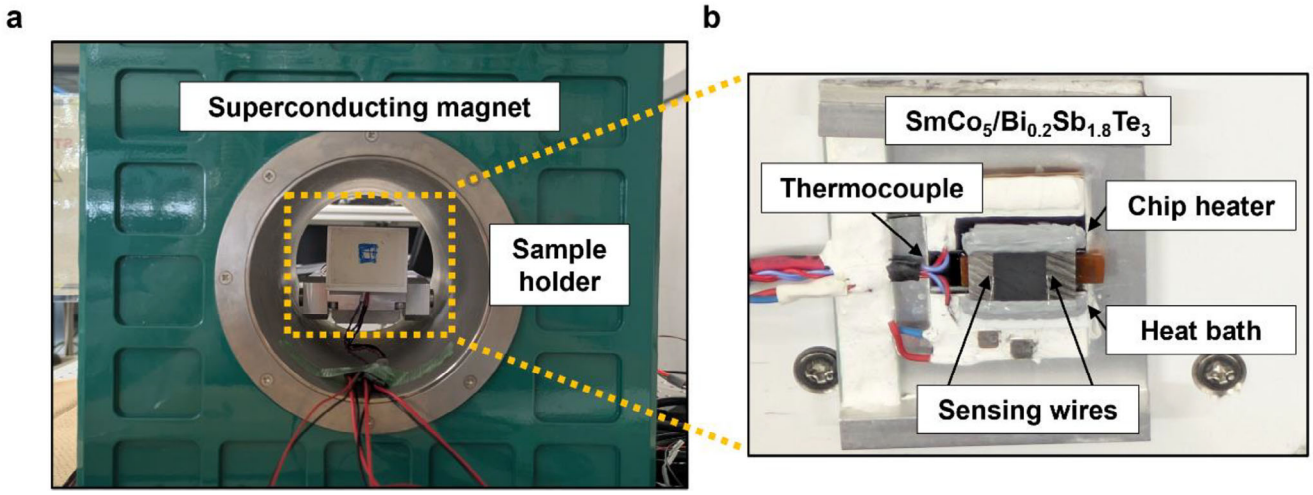

Figure 2. Experimental setup and measurement configuration. a) Photograph of the superconducting magnet used to apply a magnetic field. $SmCo_5/Bi_{0.2}Sb_{1.8}Te_3$-based ATML is mounted at the center of the bore using a custom sample holder. b) Enlarged view of the sample holder showing the $SmCo_5/Bi_{0.2}Sb_{1.8}Te_3$-based ATML fixed on Al blocks. A chip heater was placed to generate a temperature gradient across the ATML. T-type thermocouples were attached to both Al blocks to measure the temperature difference, and two sensing wires were bonded to the surface to measure the thermoelectric voltage.

Joule heating ($\propto J_c^2$). This process allows for the selective visualization of thermoelectric effects, such as the Peltier effect and anomalous Ettingshausen effect.[41,42] The A image represents the magnitude of the temperature modulation and the ϕ image provides information on the sign of the temperature modulation and the time delay due to thermal diffusion, helping to clarify the transverse thermoelectric conversion mechanism in ATMLs.[32] All LIT measurements were performed using Enhanced Lock-In Thermal Emission (ELITE, DCG Systems G.K.) at room temperature and atmospheric pressure.The LIT measurements were conducted in two configurations: cross-section configuration and top-side configuration (see Section 3.2). For measurements involving different magnetization states, the sample was magnetized in a separate superconducting magnet and then re-inserted into the LIT setup. The thermal images were aligned from successive runs by shifting them so that the $SmCo_5/Bi_{0.2}Sb_{1.8}Te_3$ interface positions overlapped, thus correcting for any slight misalignment.

The anomalous Nernst coefficient of $SmCo_5$ was also estimated using the LIT method. The LIT method enables the quantitative measurements of the temperature modulation induced by AEE; through the estimated anomalous Ettingshausen coefficient and the Onsager reciprocal relation, the anomalous Nernst coefficient can be determined.[9]

For the direct S_{xy} measurements, the sample was fixed between two anodized Al blocks. One block was connected to a heat bath while the other incorporated a chip heater, generating a temperature gradient ∇T across the sample. The surface of the sample was coated with black ink and the magnitude of ∇T was measured with the infrared camera. S_{xy} was determined by measuring the DC voltage between two Al-1%Si wires directly attached to the sample surface. The wires spanned two $SmCo_5$ layers and three $Bi_{0.2}Sb_{1.8}Te_3$ layers, ensuring that the measured S_{xy} represents an average across multiple layers. A photograph of the actual sample and experimental setup is provided in **Figure 2** to illustrate the measurement configuration. To determine σ_{xx}, four-terminal resistance measurements were carried out for the same sample. Cu wires were connected to the side surfaces of the sample, which had been coated with solder using ultrasonic soldering to ensure uniform current injection. An ac charge current with an amplitude of 10 mA was applied using a battery internal resistance tester (BT3562, Hioki E.E. Corp.) while measuring σ_{xx}. All S_{xy} and σ_{xx} measurements were performed at room temperature and atmospheric pressure.

3. Results and Discussion

3.1. Structural Optimization and Simulation of Transverse Thermoelectric Performance

To evaluate and optimize the transverse thermoelectric performance of ATML, we first measured the transport properties of the constituent materials, $SmCo_5$ and $Bi_{0.2}Sb_{1.8}Te_3$. The results are summarized in **Table 1**. The $SmCo_5$ slab used in this study exhibited a thermal conductivity κ of 12.7 ± 0.3 W m^{-1} K^{-1} and electrical conductivity σ of 1.91×10^6 S m^{-1}, while the previous sample showed higher κ of 16.8 ± 0.5 W m^{-1} K^{-1} and comparable σ of 1.80×10^6 S m^{-1}.[34] The reduced κ is expected to increase the figure of merit $z_{xy}T$ for ATML. The anomalous Nernst coefficient of $SmCo_5$ used in this study was found to be 2.9 μV K^{-1}, which is slightly smaller than but consistent with the value reported in the previous studies.[9,11,36]

To investigate the origin of the difference in κ, we analyzed the microstructure of the $SmCo_5$ slabs using EBSD. **Figure 3**

Table 1. Transport properties of $SmCo_5$ and $Bi_{0.2}Sb_{1.8}Te_3$ used in this study.

Material	σ [10^6 S m^{-1}]	κ [W m^{-1} K^{-1}]	S [μV K^{-1}]
$SmCo_5$	1.91	12.7	−19.78
$Bi_{0.2}Sb_{1.8}Te_3$	0.121	1.00	177.9

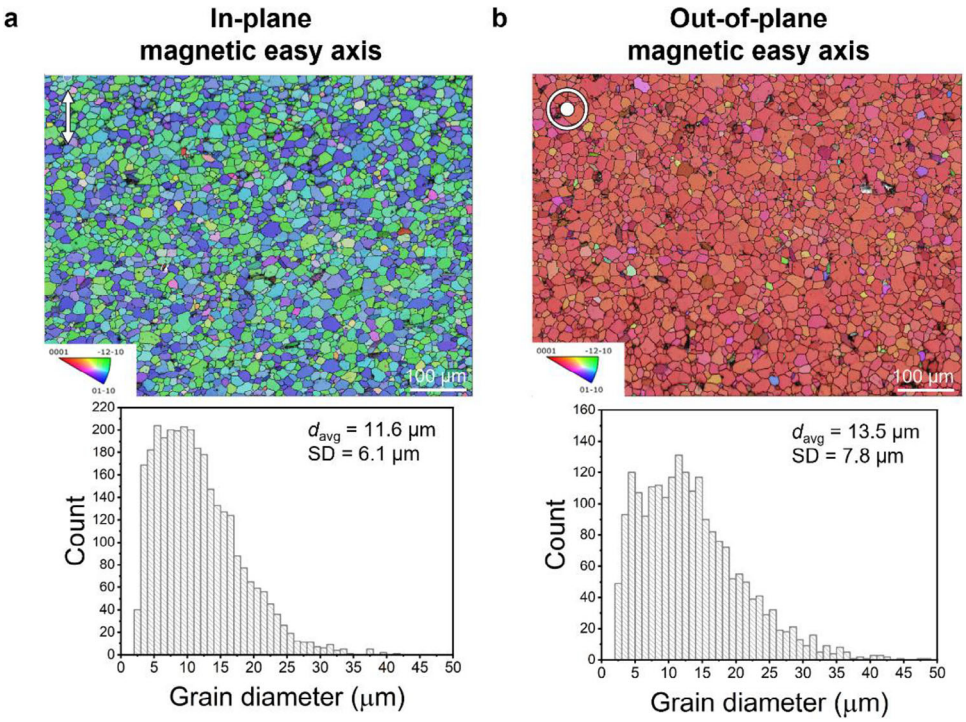

Figure 3. Electron backscatter diffraction analysis showing inverse pole figure maps of the $SmCo_5$ grains and grain size distributions of the $SmCo_5$ slabs with a) in-plane magnetic easy axis and b) out-of-plane magnetic easy axis. The direction of the magnetic easy axis is indicated by the white symbol at the top-left of each image. d_{avg} and SD denote the average grain size and standard deviation, respectively.

presents the results of the EBSD analysis showing inverse pole figure maps of the $SmCo_5$ grains and grain size distributions for the $SmCo_5$ slab with the in-plane magnetic easy axis used in this study (Figure 3a) and that with the out-of-plane magnetic easy axis used in the previous study (Figure 3b). The $SmCo_5$ slab used in this study exhibits a smaller average grain size (11.6 μm) and a narrower grain size distribution compared to the previously reported sample (13.5 μm). These microstructural differences can be one of the possible reasons for the reduced κ observed in the present sample.[43,44] While a systematic study of how grain size affects the thermal conductivity of $SmCo_5$ would be insightful, it lies beyond the scope of this work and is proposed as a direction for future research. Note that EBSD provides crystallographic orientation and grain size information, but does not probe magnetic domains; accordingly, our analysis focused on the crystallographic features, and the magnetic easy axis of the $SmCo_5$ slabs was predetermined by the supplier.

Using σ, κ, and the Seebeck coefficient S of $SmCo_5$ and $Bi_{0.2}Sb_{1.8}Te_3$, the transport properties of $SmCo_5/Bi_{0.2}Sb_{1.8}Te_3$-based ATML were simulated based on the methods of the references.[23,30] **Figure 4** shows the contour maps of σ_{xx}, κ_{yy}, S_{xy}, and $z_{xy}T$ at $T = 300$ K as functions of the tilt angle θ and thickness ratio $t = t_{SmCo}/(t_{SmCo}+t_{BST})$, where $t_{SmCo(BST)}$ is the thickness of the $SmCo_5$ ($Bi_{0.2}Sb_{1.8}Te_3$) layer. The optimized $z_{xy}T$ value for ODSE in $SmCo_5/Bi_{0.2}Sb_{1.8}Te_3$-based ATML reaches 0.30 at room temperature when $\theta = 25°$ and $t = 0.50$. This significant improvement of $z_{xy}T$ compared to that reported in Ref. [34] is attributed mainly to the aforementioned difference in the transport properties of the $SmCo_5$ slabs. $SmCo_5/Bi_{0.2}Sb_{1.8}Te_3$-based ATML was designed and synthesized to optimize ODSE based on the calculation result. The experimentally realized θ and t of $SmCo_5/Bi_{0.2}Sb_{1.8}Te_3$-based ATML were estimated to be $25 \pm 2°$ and 0.41 ± 0.02, respectively. The individual thicknesses of the $SmCo_5$ and $Bi_{0.2}Sb_{1.8}Te_3$ layers were 0.476 ± 0.017 mm and 0.691 ± 0.066 mm. The tilt angle and thickness ratio were determined from real-space images acquired by an infrared camera, with a spatial resolution of 15 μm per pixel. The corresponding $z_{xy}T$ value was calculated to be 0.29, showing that $SmCo_5/Bi_{0.2}Sb_{1.8}Te_3$-based ATML with almost optimized $z_{xy}T$ was synthesized, as shown by red points in Figure 4.

3.2. Observation of Giant Off-Diagonal Peltier Effect

Here, we visualize the ODPE and AEE signals as temperature modulation in the following LIT measurements, whereas the ODSE and ANE signals shown in Section 3.4 are measured separately as transverse voltages. **Figure 5** displays the results of the LIT measurements for demagnetized $SmCo_5/Bi_{0.2}Sb_{1.8}Te_3$-based ATML. The A and ϕ images at different lock-in frequencies (f = 10.0, 1.0, and 0.1 Hz) in the cross-section configuration are shown in Figure 5a,b. At $f = 10.0$ Hz, heating and cooling signals are localized near the junction interfaces between $SmCo_5$ and $Bi_{0.2}Sb_{1.8}Te_3$, where the A signals peak along the oblique interfaces (Figure 5c) and the ϕ image exhibits a 180° phase reversal between neighboring interfaces (Figure 5d), consistent with Peltier-effect-induced temperature modulation as previously reported in similar ATML systems.[32–34] Unlike conventional

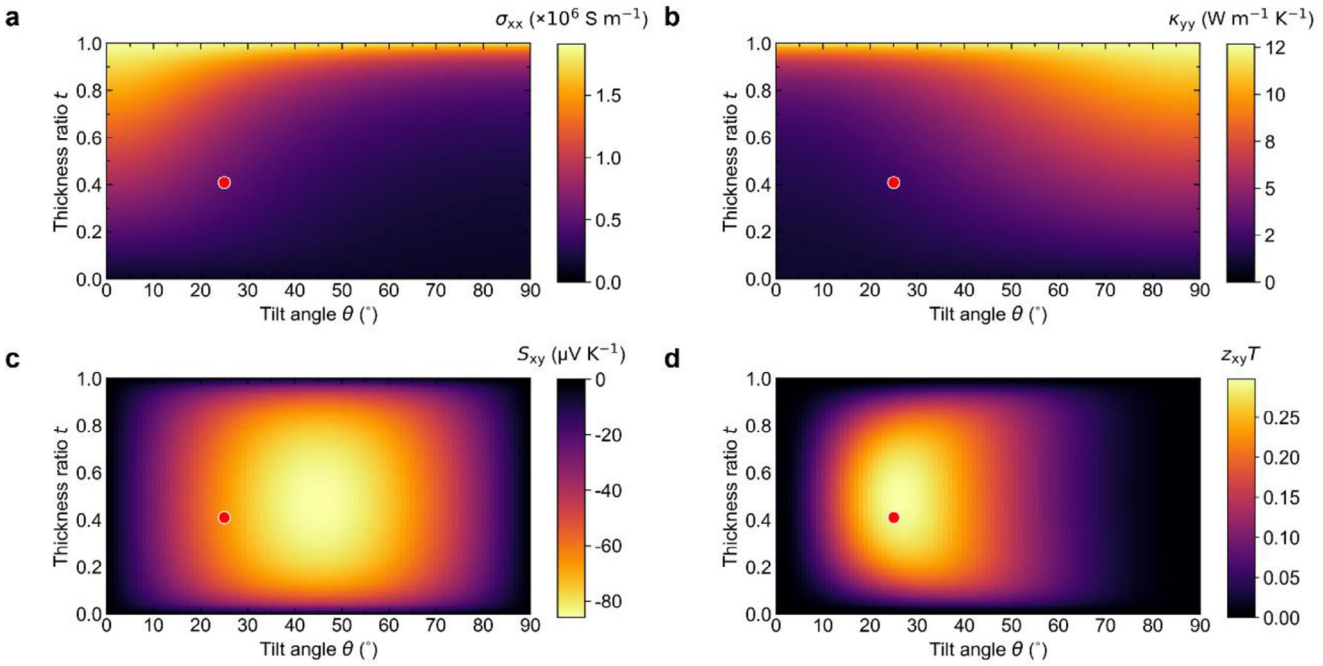

Figure 4. Contour maps of the transport properties as functions of the tilt angle θ and thickness ratio t in $SmCo_5/Bi_{0.2}Sb_{1.8}Te_3$-based ATML at 300 K: a) electrical conductivity along the x direction σ_{xx}, b) thermal conductivity along the y direction κ_{yy}, c) transverse thermopower S_{xy}, and d) transverse figure of merit $z_{xy}T$. The red points correspond to the θ and t values for the sample used in this study, i.e., $\theta = 25°$ and $t = 0.41$.

Peltier-effect-induced temperature modulation at non-oblique interfaces,[45,46] the magnitude of the A signals is non-uniform along the oblique interfaces due to the non-uniform J_c flow within the ATML structure, confirming the transverse thermoelectric conversion originating from ODPE. As f decreases to 0.1 Hz, approaching a nearly steady-state, thermal diffusion broadens the heating and cooling signals. The ϕ signals range from ≈0° (lower side of the sample) to 180° (upper side of the sample) in the direction perpendicular to J_c, indicating transverse thermoelectric heating and cooling induced by ODPE, respectively. The x-directional profiles of A and ϕ further reveal periodic variations due to the multilayer structure (Figure 5e,f). The transverse thermoelectric cooling behavior is more distinctly observed in the top-side configuration, as demonstrated in Figure 5i–p.

To estimate the transverse thermoelectric heating and cooling performance of $SmCo_5/Bi_{0.2}Sb_{1.8}Te_3$-based ATML, the LIT results were averaged over one $SmCo_5/Bi_{0.2}Sb_{1.8}Te_3$ unit. Figure 5g,h (5o,p) shows the f dependence of the averaged A and ϕ values, i.e., A_{ave} and ϕ_{ave}, for one $SmCo_5/Bi_{0.2}Sb_{1.8}Te_3$ unit in the cross-section (top-side) configuration. The corresponding averaged areas are defined by the white rectangles in Figure 5c,d (5k,l). The magnitude of A_{ave} monotonically increases as f decreases while ϕ_{ave} gradually shifts toward 180°, approaching the steady-state temperature distribution. Notably, the A_{ave} value at f = 0.1 Hz for present $SmCo_5/Bi_{0.2}Sb_{1.8}Te_3$-based ATML is over 10 times (≈1.5 times) larger than that of $Nd_2Fe_{14}B/Bi_{88}Sb_{12}$-based ATML (conventional $SmCo_5/Bi_{0.2}Sb_{1.8}Te_3$-based ATML) used in the previous studies.[32,34] These observations provide direct evidence that present $SmCo_5/Bi_{0.2}Sb_{1.8}Te_3$-based ATML exhibits enhanced transverse thermoelectric performance due to its optimized material and structural design, further confirming its superiority over previously reported ATML systems.

3.3. Separation of Anomalous Ettingshausen Effect from Off-Diagonal Peltier Effect

Next, we separately visualize the contributions of ODPE and AEE in magnetized $SmCo_5/Bi_{0.2}Sb_{1.8}Te_3$-based ATML. To magnetize the $SmCo_5$ layers, the magnetic field $\mu_0 H = \pm 5.0$ T, where μ_0 and H are the vacuum permeability and magnitude of the magnetic field, respectively, was applied along the z direction (Figure 1) before the LIT measurements (note that 5.0 T is larger than the coercivity of the $SmCo_5$ slabs). The magnetization (M)-even-dependent component represents temperature modulation that does not change with the M reversal, such as ODPE and its modulation by the H and/or M dependence of σ, κ, and S, while the M-odd-dependent component captures effects that change with the M reversal, characteristic of AEE. To separate the ODPE and AEE contributions, the M-even- and M-odd-dependent components of the LIT signals were extracted using the following equations:

$$A_{even} = \left| A(+M)\, e^{-i\phi(+M)} + A(-M)\, e^{-i\phi(-M)} \right| / 2 \quad (1)$$

$$\phi_{even} = -\arg\left[A(+M)\, e^{-i\phi(+M)} + A(-M)\, e^{-i\phi(-M)} \right] \quad (2)$$

$$A_{odd} = \left| A(+M)\, e^{-i\phi(+M)} - A(-M)\, e^{-i\phi(-M)} \right| / 2 \quad (3)$$

$$\phi_{odd} = -\arg\left[A(+M)\, e^{-i\phi(+M)} - A(-M)\, e^{-i\phi(-M)} \right] \quad (4)$$

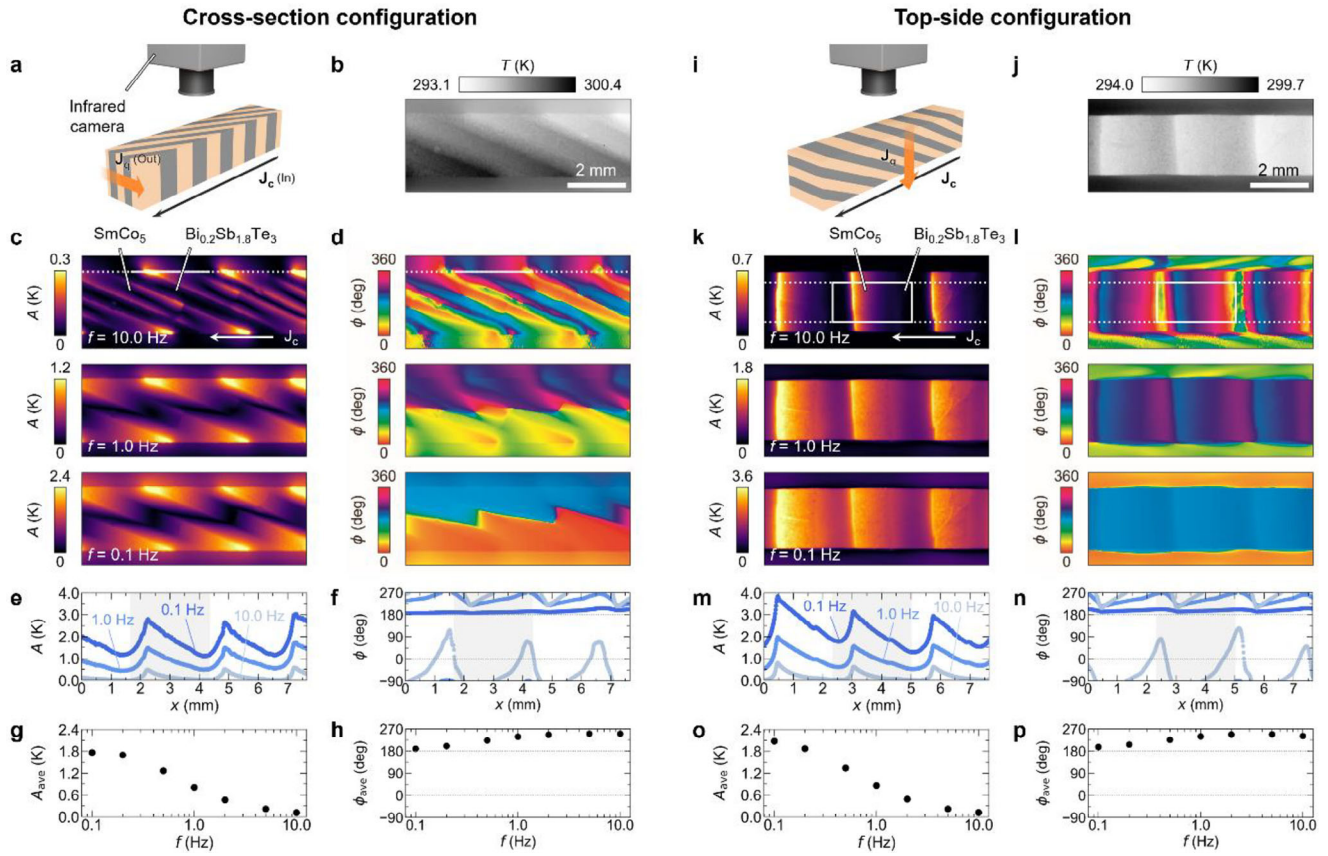

Figure 5. Transverse thermoelectric conversion in demagnetized $SmCo_5/Bi_{0.2}Sb_{1.8}Te_3$-based ATML. a) Schematic of the sample structure in the cross-section configuration. b) Steady-state temperature image during the LIT measurement in the cross-section configuration. c,d) Lock-in amplitude A (c) and phase ϕ (d) images at the lock-in frequencies of $f = 10.0$, 1.0, and 0.1 Hz. e,f) x-directional A (e) and ϕ (f) profiles along the white dotted lines in the top panels of c and d, respectively. g,h) f dependence of the averaged lock-in amplitude A_{ave} (g) and phase ϕ_{ave} (h) values over one $SmCo_5/Bi_{0.2}Sb_{1.8}Te_3$ unit. i–p) Results for the top-side configuration. The A_{ave} and ϕ_{ave} values in g and h (o and p) were estimated by averaging A and ϕ signals in the areas defined by the white rectangles in c and d (k and l), corresponding to the gray shaded area in e and f (m and n), respectively. In all the LIT measurements, a square-wave-modulated ac charge current with an amplitude of 1 A and zero offset was applied.

where A_{even} (A_{odd}) and ϕ_{even} (ϕ_{odd}) represent the lock-in amplitude and phase exhibiting the M-even (M-odd) dependence. $A(+M)$ [$\phi(+M)$] and $A(-M)$ [$\phi(-M)$] are defined as A (ϕ) measured when the magnetization vector $\mathbf{M}$ is along the $+z$ and $-z$ directions, respectively. Importantly, no external magnetic field was applied during the LIT measurements, meaning that AEE occurs due to the remanent magnetization of the $SmCo_5$ slabs.

Figure 6a,b shows the A_{even} and ϕ_{even} images at different f values (10.0, 1.0, and 0.1 Hz) in the top-side configuration. The periodic heating and cooling signals along the multilayer interfaces confirm the presence of ODPE, consistent with Figure 5. The magnitude of the A_{even} signals were found to be comparable to those observed in the demagnetized sample, confirming the minor role of the magnetoresistance, magneto-thermal resistance, and magneto-Peltier effect in the ODPE signals.

The M-odd-dependent component, which isolates the AEE contribution, is shown in Figure 6e,f. The temperature distribution localized in the $SmCo_5$ regions defined by the gray rectangle at $f = 10.0$ Hz confirms the existence of the AEE contribution in $SmCo_5$ even in the absence of an applied magnetic field. The f dependence of A_{odd} (Figure 6g) shows an increasing trend at lower f, similar to the ODPE case, while the ϕ_{odd} (Figure 6h) remains close to 180°, indicating that the transverse thermoelectric cooling also occurs in the M-odd-dependent component. A substantial magnitude of A_{odd} was also observed in the $Bi_{0.2}Sb_{1.8}Te_3$ regions defined by the orange rectangle. However, the A_{odd} signals at $f = 10$ Hz is strongly localized in the $SmCo_5$ regions, while ϕ_{odd} in the $Bi_{0.2}Sb_{1.8}Te_3$ regions gradually shifts toward 180° as f decreases. This suggests that the $Bi_{0.2}Sb_{1.8}Te_3$ do not act as an independent heat source and the observed A_{odd} signals in the $Bi_{0.2}Sb_{1.8}Te_3$ regions arise primarily from heat diffusion driven by AEE in the $SmCo_5$ regions. Because all LIT measurements in this study were performed in the absence of an external magnetic field, the contribution of the ordinary Ettingshausen effect in the $Bi_{0.2}Sb_{1.8}Te_3$ is negligible under the present conditions. These clear observations of both ODPE and AEE without an external magnetic field highlight a significant advantage of in-plane magnetized $SmCo_5/Bi_{0.2}Sb_{1.8}Te_3$-based ATML over previous systems that required an external magnetic field to induce ANE.

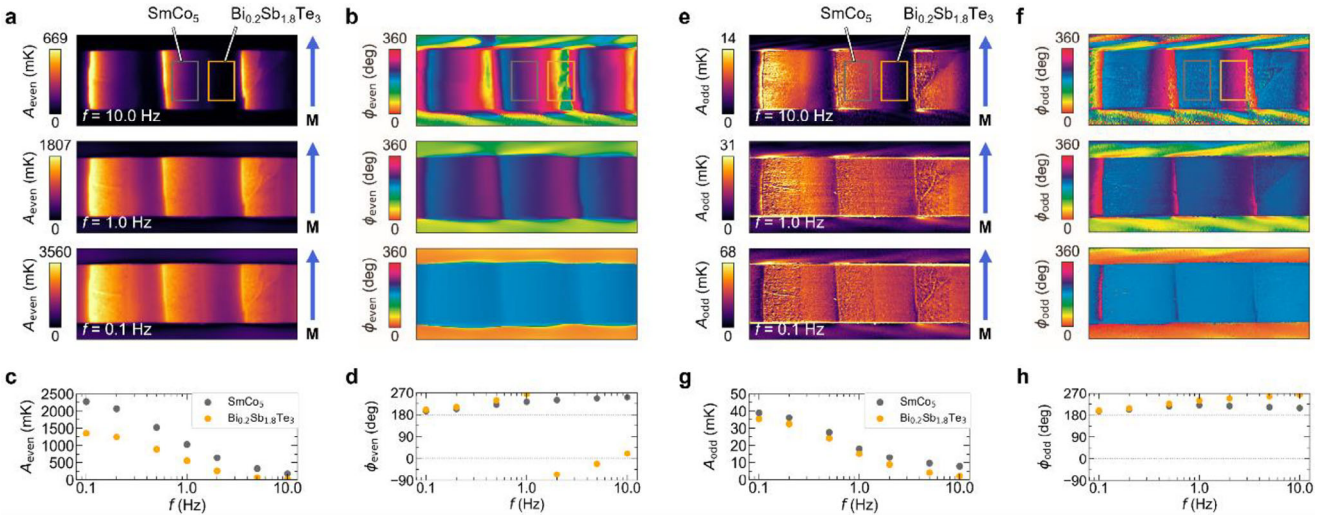

Figure 6. Contributions of ODPE and AEE in $SmCo_5/Bi_{0.2}Sb_{1.8}Te_3$-based ATML in the top-side configuration. a,b) *M*-even-dependent component of the lock-in amplitude A_{even} (a) and phase ϕ_{even} (b) images at $f =$ 10.0, 1.0, and 0.1 Hz. c,d) f dependence of A_{even} (c) and ϕ_{even} (d). e–h) Results for the *M*-odd-dependent component: A_{odd} and ϕ_{odd}. The magnetic field with $\mu_0 H = \pm 5.0$ T was applied along the z direction (Figure 1) to magnetize the sample before the LIT measurements. μ_0 and **M** represent the vacuum permeability and spontaneous magnetization of the $SmCo_5$-type magnets, respectively. The data points in c and d (g and h) were obtained by averaging A_{even} and ϕ_{even} (A_{odd} and ϕ_{odd}) signals in the areas defined by the gray and orange rectangles in a and b (e and f), respectively. All the LIT data in this figure were measured in the absence of an external magnetic field.

3.4. Performance of Hybrid Transverse Thermoelectric Conversion

To investigate the total transverse thermoelectric performance in $SmCo_5/Bi_{0.2}Sb_{1.8}Te_3$-based ATML, we experimentally measured σ_{xx} and S_{xy} and determined $z_{xy}T$. A crucial factor of complex thermoelectric materials is the interfacial resistance between constituent layers, which can significantly impact transport properties. However, as reported in the previous report,[34] the interfacial electrical and thermal resistances between $SmCo_5$ and $Bi_{0.2}Sb_{1.8}Te_3$ were found to be negligible, confirming that the two materials are well bonded without significant interfacial resistances. Furthermore, magnetic property measurements confirmed that the $SmCo_5$ layers retained their permanent magnet characteristics even after sinter-bonding with $Bi_{0.2}Sb_{1.8}Te_3$. The $SmCo_5$ layers exhibited a large remanent magnetization of 0.84 T and coercivity of 2.95 T, as shown in the top panel of **Figure** 7a. This result ensures that $SmCo_5/Bi_{0.2}Sb_{1.8}$Te-based ATML functions as a permanent magnet, enabling magnetic-field-free hybrid transverse thermoelectric operation.

For a precise assessment of the thermoelectric performance arising from the hybrid action of ODSE and ANE, we applied a temperature difference ΔT between the top and bottom surfaces of ATML and measured the transverse thermoelectric voltage V under an external magnetic field with $\mu_0 H = \pm 5.0$ T, as shown in the inset of Figure 7b. The magnetization curve in the top panel of Figure 7a and the H dependence of V in the bottom panel of Figure 7a exhibit a similar trend, confirming the correlation between the magnetic and thermoelectric responses. The transverse thermoelectric voltage follows the hysteretic behavior of magnetization, demonstrating the presence of the ANE-induced transverse thermoelectric output that changes with magnetization reversal. The *V*-*H* curves in the bottom panel of Figure 7a also exhibit the symmetric contribution with respect to H; this can be explained by the *M*-even-dependent component, such as the magnetoresistance, magneto-thermal resistance, and magneto-Peltier effect, superimposed on the transverse thermoelectric conversion.

The thermopower measurements in Figure 7b determine S_{xy} to be $-70.7 \pm 0.6\ \mu V\ K^{-1}$ ($-72.1 \pm 0.6\ \mu V\ K^{-1}$) at 0 T after aligning **M** along the $+z$ ($-z$) direction, which is represented by $+\mathbf{M}$ ($-\mathbf{M}$). Interestingly, the experimentally obtained values of S_{xy} exceeded the calculated value of $-65.5\ \mu V\ K^{-1}$, likely due to the contribution of off-diagonal thermal conduction in the adiabatic condition, consistent with observations in a previous report.[47] In addition, we measured the ac resistance of ATML, obtaining a value of 1.46 mΩ, which was slightly higher than the calculated resistance of 1.23 mΩ from the simulated σ_{xx} and the sample geometry. Using this measured resistance, we determined σ_{xx} of the sample. The slightly lower σ_{xx} may be attributed to microstructural factors such as cracks introduced in $SmCo_5$ during the sintering process. Based on the measured σ_{xx} and S_{xy} values and simulated κ_{yy}, we estimated $z_{xy}T$ to be 0.288 ± 0.005 at $+\mathbf{M}$ and 0.299 ± 0.005 at $-\mathbf{M}$. Although the difference in $z_{xy}T$ between the $+\mathbf{M}$ and $-\mathbf{M}$ configurations appears modest, it is important that this variation originates from ANE. The resulting 3.9% change in $z_{xy}T$, corresponding to an increase of 0.011, is significantly larger than the figure of merit of ANE alone for $SmCo_5$, which is smaller than 0.001 at room temperature. This clearly demonstrates that the cross term $2S_{ODSE}\hat{S}_{ANE}$, introduced by the hybridization of ODSE and ANE, plays a crucial role in enhancing the overall transverse thermoelectric performance. Despite the lower σ_{xx}, the higher measured S_{xy} compensated for this reduction, resulting in the $z_{xy}T$ values comparable to the analytical prediction in Figure 4d. Most importantly, this experimentally evaluated $z_{xy}T$ value reaching ≈0.3 represents a record-high performance for transverse thermoelectric

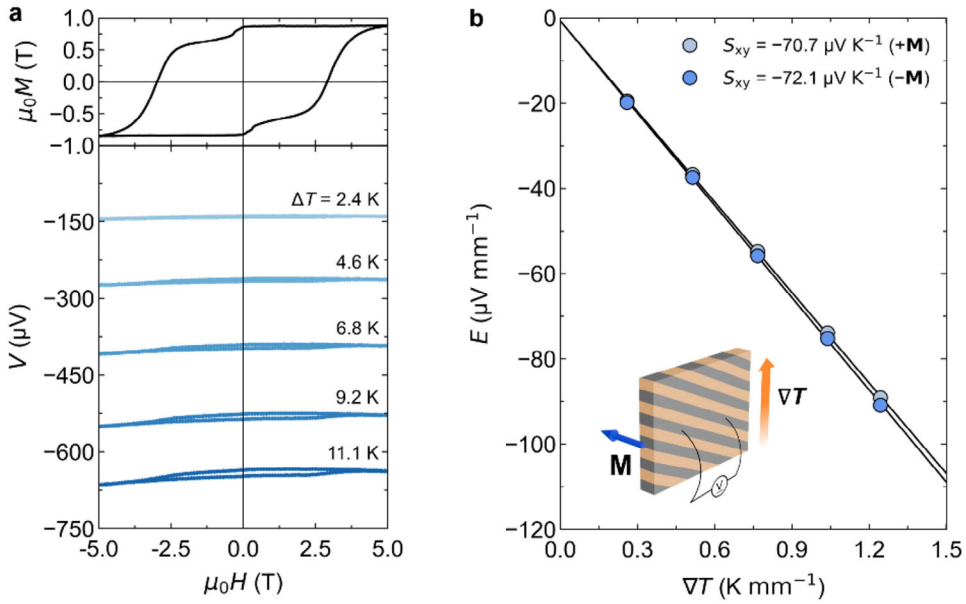

Figure 7. Hybrid transverse thermoelectric generation in $SmCo_5/Bi_{0.2}Sb_{1.8}Te_3$-based ATML. a) H dependence of the magnetization M of the $SmCo_5$-type magnets (top panel of a) and transverse thermoelectric voltage V at various ΔT values (bottom panel of a). The M-H curve was measured by vibrating sample magnetometry. ΔT denotes the temperature difference between the top and bottom surfaces of the sample. b) Temperature gradient ∇T dependence of the transverse electric field E. The transverse thermopower S_{xy} was estimated to be −70.7 μV K^{-1} (−72.1 μV K^{-1}) at 0 T after aligning **M** along the $+z$ ($-z$) direction, which is represented by +**M** (−**M**). The inset shows a schematic of the setup for measuring the transverse thermopower.

conversion around room temperature, surpassing previously reported values for transverse thermoelectric materials.[34]

4. Conclusion

We demonstrated a high-performance, magnetic-field-free hybrid transverse thermoelectric conversion using $SmCo_5/Bi_{0.2}Sb_{1.8}Te_3$-based ATMLs. By leveraging the spontaneous magnetization of $SmCo_5$, we successfully induced ANE in ATML without applying an external magnetic field. Through LIT measurements and direct thermoelectric property characterization, we observed enhanced transverse thermoelectric performance driven by the hybridization of ODSE and ANE. Although ODSE dominates the overall output, ANE introduces a magnetization-direction-dependent component, enabling magnetically switchable thermoelectric conversion. This switchable functionality, coupled with the intrinsic performance enhancement from hybridization, adds a valuable degree of control for future applications of transverse thermoelectrics. The optimized ATML structure exhibited a transverse figure of merit $z_{xy}T$ of ≈0.3 at room temperature, setting a new benchmark for hybrid transverse thermoelectric materials. Our results highlight the potential of ATMLs comprising permanent magnets as a promising platform for energy harvesting and thermal management applications, particularly in scenarios requiring stable, high-performance thermoelectric conversion without continuous magnetic field application. Future work should focus on finding and developing permanent magnets with giant ANE as well as further improving the performance of ODSE through the optimization of material combination, composition, microstructural design, and interface structures.

Acknowledgements

The authors thank K. Suzuki and M. Isomura for technical support. This work was supported by ERATO "Magnetic Thermal Management Materials" (No. JPMJER2201) from Japan Science and Technology Agency (JST) and Grant-in-Aid for Early-Career Scientists (KAKENHI) (No. 24K17610) from Japan Society for the Promotion of Science (JSPS).

Conflict of Interest

The authors declare no conflict of interest.

Data Availability Statement

The data that support the findings of this study are available from the corresponding author upon reasonable request.

Keywords

anomalous Nernst effect, artificially tilted multilayer, off-diagonal Seebeck effect, permanent magnet, transverse thermoelectrics

Received: March 28, 2025
Revised: June 15, 2025
Published online: June 29, 2025

[1] D. M. Rowe, *Thermoelectrics Handbook: Macro to Nano*, CRC Press, New York, USA, **2006**.
[2] L. E. Bell, *Science* **2008**, *321*, 1457.
[3] G. J. Snyder, E. S. Toberer, *Nat. Mater.* **2008**, *7*, 105.

[4] Q. Yan, M. G. Kanatzidis, *Nat. Mater.* **2022**, *21*, 503.
[5] K. Uchida, J. P. Heremans, *Joule* **2022**, *6*, 2240.
[6] A. v. Ettingshausen, W. Nernst, *Ann. Phys.* **1886**, *265*, 343.
[7] Y. Sakuraba, *Scr. Mater.* **2016**, *111*, 29.
[8] A. Sakai, Y. P. Mizuta, A. A. Nugroho, R. Sihombing, T. Koretsune, M.-T. Suzuki, N. Takemori, R. Ishii, D. Nishio-Hamane, R. Arita, P. Goswami, S. Nakatsuji, *Nat. Phys.* **2018**, *14*, 1119.
[9] A. Miura, H. Sepehri-Amin, K. Masuda, H. Tsuchiura, Y. Miura, R. Iguchi, Y. Sakuraba, J. Shiomi, K. Hono, K. Uchida, *Appl. Phys. Lett.* **2019**, *115*, 222403.
[10] A. Sakai, S. Minami, T. Koretsune, T. Chen, T. Higo, Y. Wang, T. Nomoto, M. Hirayama, S. Miwa, D. Nishio-Hamane, F. Ishii, R. Arita, S. Nakatsuji, *Nature* **2020**, *581*, 53.
[11] A. Miura, K. Masuda, T. Hirai, R. Iguchi, T. Seki, Y. Miura, H. Tsuchiura, K. Takanashi, K. Uchida, *Appl. Phys. Lett.* **2020**, *117*, 082408.
[12] K. Uchida, W. Zhou, Y. Sakuraba, *Appl. Phys. Lett.* **2021**, *118*, 140504.
[13] Y. Pan, C. Le, B. He, S. J. Watzman, M. Yao, J. Gooth, J. P. Heremans, Y. Sun, C. Felser, *Nat. Mater.* **2022**, *21*, 203.
[14] B. He, Y. Wang, M. Q. Arguilla, N. D. Cultrara, M. R. Scudder, J. E. Goldberger, W. Windl, J. P. Heremans, *Nat. Mater.* **2019**, *18*, 568.
[15] M. R. Scudder, B. He, Y. Wang, A. Rai, D. G. Cahill, W. Windl, J. P. Heremans, J. E. Goldberger, *Energy Environ. Sci.* **2021**, *14*, 4009.
[16] M. R. Scudder, K. G. Koster, J. P. Heremans, J. E. Goldberger, *Appl. Phys. Rev.* **2022**, *9*, 021420.
[17] Y. Goto, H. Usui, M. Murata, J. E. Goldberger, J. P. Heremans, C.-H. Lee, *Chem. Mater.* **2024**, *36*, 2018.
[18] H. Manako, S. Ohsumi, Y. J. Sato, R. Okazaki, D. Aoki, *Nat. Commun.* **2024**, *15*, 3907.
[19] T. Zahner, R. Förg, H. Lengfellner, *Appl. Phys. Lett.* **1998**, *73*, 1364.
[20] A. Kyarad, H. Lengfellner, *Appl. Phys. Lett.* **2006**, *89*, 192103.
[21] T. Kanno, S. Yotsuhashi, A. Sakai, K. Takahashi, H. Adachi, *Appl. Phys. Lett.* **2009**, *94*, 061917.
[22] C. Reitmaier, F. Walther, H. Lengfellner, *Appl. Phys. A* **2010**, *99*, 717.
[23] H. J. Goldsmid, *J. Electron. Mater.* **2011**, *40*, 1254.
[24] T. Kanno, A. Sakai, K. Takahashi, A. Omote, H. Adachi, Y. Yamada, *Appl. Phys. Lett.* **2012**, *101*, 011906.
[25] T. Kanno, K. Takahashi, A. Sakai, H. Tamaki, H. Kusada, Y. Yamada, *J. Electron. Mater.* **2014**, *43*, 2072.
[26] A. Sakai, T. Kanno, K. Takahashi, H. Tamaki, H. Kusada, Y. Yamada, H. Abe, *Sci. Rep.* **2014**, *4*, 6089.
[27] X. Mu, H. Zhou, W. Zhao, D. He, W. Zhu, X. Nie, Z. Sun, Q. Zhang, *J. Power Sources* **2019**, *430*, 193.
[28] Y. Li, P. Wei, H. Zhou, X. Mu, W. Zhu, X. Nie, X. Sang, W. Zhao, *J. Electron. Mater.* **2020**, *49*, 5980.
[29] W. Zhu, X. Guo, X. Sang, P. Wei, X. Nie, W. Zhao, Q. Zhang, *J. Power Sources* **2021**, *512*, 230471.
[30] H. Zhou, H. Liu, G. Qian, H. Yu, X. Gong, X. Li, J. Zheng, *Micromachines* **2022**, *13*, 233.
[31] K. Yue, W. Zhu, Q. He, X. Nie, X. Qi, C. Sun, W. Zhao, Q. Zhang, *ACS Appl. Mater. Interfaces* **2022**, *14*, 39053.
[32] K. Uchida, T. Hirai, F. Ando, H. Sepehri-Amin, *Adv. Energy Mater.* **2024**, *14*, 2302375.
[33] T. Hirai, F. Ando, H. Sepehri-Amin, K. Uchida, *Nat. Commun.* **2024**, *15*, 9643.
[34] F. Ando, T. Hirai, A. Alasli, H. Sepehri-Amin, Y. Iwasaki, H. Nagano, K. Uchida, *Energy Environ. Sci.* **2025**, *18*, 4068.
[35] R. Modak, Y. Sakuraba, T. Hirai, T. Yagi, H. Sepehri-Amin, W. Zhou, H. Masuda, T. Seki, K. Takanashi, T. Ohkubo, K. Uchida, *Sci. Technol. Adv. Mater.* **2022**, *23*, 767.
[36] F. Ando, T. Hirai, K. Uchida, *APL Energy* **2024**, *2*, 016103.
[37] M. Murata, T. Hirai, T. Seki, K. Uchida, *Appl. Phys. Lett.* **2024**, *124*, 193901.
[38] O. Breitenstein, W. Warta, M. Langenkamp, *Lock-in Thermography: Basics and Use for Evaluating Electronic Devices and Materials*, Springer, Berlin, Heidelberg, Germany, **2010**.
[39] S. Daimon, R. Iguchi, T. Hioki, E. Saitoh, K. Uchida, *Nat. Commun.* **2016**, *7*, 13754.
[40] K. Uchida, S. Daimon, R. Iguchi, E. Saitoh, *Nature* **2018**, *558*, 95.
[41] T. Seki, R. Iguchi, K. Takanashi, K. Uchida, *Appl. Phys. Lett.* **2018**, *112*, 152403.
[42] R. Das, R. Iguchi, K. Uchida, *Phys. Rev. Appl.* **2019**, *11*, 034022.
[43] K. Kishimoto, T. Koyanagi, *J. Appl. Phys.* **2002**, *92*, 2544.
[44] D.-H. Kim, T. Mitani, *J. Alloys Compd.* **2005**, *399*, 14.
[45] H. Straube, J.-M. Wagner, O. Breitenstein, *Appl. Phys. Lett.* **2009**, *95*, 052107.
[46] A. Alasli, T. Hirai, H. Nagano, K. Uchida, *Appl. Phys. Lett.* **2022**, *121*, 154104.
[47] F. Ando, T. Hirai, H. Adachi, K. Uchida, *Phys. Rev. Appl.* **2025**, *23*, 064061.